REMUNOM
ISSN 2178-6925

Received: 13/10/2026 - **Accepted:** 12/11/2026
Vol: 13.23
DOI: 10.66104/sdhm5c86
Pages: 1-29

COUPLED ELECTRO-THERMAL AND STORAGE DYNAMICS OF AM0 PHOTOVOLTAIC SYSTEMS SUPPLYING MEGAWATT-SCALE SPACE DATA CENTERS: A SIMULATION-BASED DESIGN STUDY

DINÂMICA ELETROTÉRMICA E DE ARMAZENAMENTO ACOPLADA DE SISTEMAS FOTOVOLTAICOS AM0 PARA CENTROS DE DADOS ESPACIAIS EM ESCALA MEGAWATT: UM ESTUDO DE PROJETO BASEADO EM SIMULAÇÃO

DINÁMICA ELECTROTÉRMICA Y DE ALMACENAMIENTO ACOPLADA DE SISTEMAS FOTOVOLTAICOS AM0 PARA CENTROS DE DATOS ESPACIALES A ESCALA MEGAVATIO: UN ESTUDIO DE DISEÑO BASADO EN SIMULACIÓN

Dafnhê Thor Castro de Martins Barros
Mestrando em Engenharia de Controle e Automação (PROPECAUT) — Instituto Federal do Espírito Santo (IFES), Campus Serra.
Técnico de Manutenção Elétrica — Petróleo Brasileiro S.A. (Petrobras).
ORCID: 0009-0002-3904-8736
E-mail: dafnhe.thor@msn.com

Prof. Dr. Flávio Barros Braz da Silva
Doutor em Engenharia Elétrica, Professor Permanente do Programa de Pós-Graduação em Engenharia de Controle e Automação (PROPECAUT) — Instituto Federal do Espírito Santo (IFES), Campus Serra.
ORCID: 0000-0002-5304-4066
E-mail: flavio.braz@ifes.edu.br

Abstract

This paper presents an exploratory simulation-based design study of a 1 MW electrical power subsystem (EPS) for a conceptual space data center in sun-synchronous low Earth orbit (SSO-LEO). The architecture integrates a 3850 m² triple-junction photovoltaic array, a 2.5 MWh battery energy storage system (BESS), and a 400 V HVDC bus supplying constant-power computing loads (CPL). The photovoltaic model is calibrated to 1.6872 MW under 25 °C AM0 reference. Periodic orbital thermal cycling (-92.6 °C to +54.1 °C, with a 144.3 K/min exit transient) reduces sunlight energy collection to 1.5972 MWh against a continuous-operation requirement of 1.6627 MWh (operating generation dropping to 1.5509 MW), yielding an orbital energy margin of -3.9% and an analytical preliminary scaled area of 4008 m² (+4.1%). Thus, while 3850 m² serves as the unadjusted standard reference baseline at 25 °C AM0, the final recommended operational flight array aperture is 4008 m² to ensure full energy closure under hot-orbit conditions. In the post-eclipse tracking window, temperature-compensated predictive MPPT (TC-PMPPT) achieves 98.46% tracking efficiency (+4.78 pp over nominal P&O at T_s = 1.0 s), demonstrating reduced step-size sensitivity across parameter sweeps rather than universal efficiency dominance, as tuned classic methods match it at fast sampling (T_s = 0.2 s). For battery state estimation, selective innovation-driven adaptation restricted to the ohmic resistance process-noise channel ($Q(R_0)$) prevents covariance divergence, achieving zero non-finite runs across an extensive 500-seed Monte Carlo evaluation (0.00% divergence rate vs 8.80% for full-covariance fading UKF) and a high-precision nominal state-of-charge RMSE of 0.297% ± 0.039%. For bus stability, undamped constant-power loads precipitate Middlebrook instability; parallel RC damping with $n \geq 4$ satisfies the 6 dB impedance margin. Large-signal 1.0 to 2.2 MW step simulations show that a transient nadir of 344.7 V (55.3 V dip) drives instantaneous load current to 6.38 kA (exceeding the 6.0 kA converter limit), but the system recovers without collapse because the damping capacitor bank

CC BY

REMUNOM
ISSN 2178-6925

Received: 13/10/2026 - **Accepted:** 12/11/2026
Vol: 13.23
DOI: 10.66104/sdhm5c86
Pages: 1-29

supplies the transient deficit current. A 2 kHz PI controller with feedforward achieves the best dynamic recovery. In the equal-power dry mass budget, total mass is reduced by 62.8% (from 46,712 kg to 17,360 kg, saving 29,352 kg), of which 5.16 t is directly attributable to the 400 V bus and GaN conversion. Planar laminated busbars and dynamic charge-recovery hold-up bounds limit required capacitance to 32.5--35.0 mF, far below unoptimized reactive estimates.

Keywords: AM0 photovoltaics; Constant-power load; High-voltage space bus; Maximum power point tracking; Orbital data centers; Square-root unscented Kalman filter.

Resumo

Este artigo apresenta um estudo exploratório de projeto baseado em simulação de um subsistema de potência elétrica (EPS) de 1 MW para um centro de dados espacial conceitual em órbita baixa da Terra heliossíncrona (SSO-LEO). A arquitetura integra um arranjo fotovoltaico de tripla junção de 3850 m², um sistema de armazenamento de energia em baterias (BESS) de 2,5 MWh e um barramento de 400 V HVDC alimentando cargas computacionais de potência constante (CPL). O modelo fotovoltaico é calibrado para 1,6872 MW na condição de referência AM0 a 25 °C. A ciclagem térmica orbital periódica (-92,6 °C a +54,1 °C, com transiente de saída de penumbra de 144,3 K/min) reduz a coleta de energia solar para 1,5972 MWh frente a uma exigência operacional de 1,6627 MWh (potência em regime quente decaindo para 1,5509 MW), resultando em uma margem energética orbital de -3,9% e indicando uma área analítica preliminar redimensionada de 4008 m² (+4,1%). Assim, enquanto 3850 m² serve como área de referência padrão a 25 °C AM0, a área final recomendada para operação de voo é de 4008 m² para fechamento energético completo sob condições orbitais quentes. Na janela de rastreamento pós-eclipse, o algoritmo MPPT preditivo compensado em temperatura (TC-PMPPT) atinge 98,46% de eficiência (+4,78 pp sobre o P&O nominal em T_s = 1,0 s), demonstrando menor sensibilidade aos parâmetros de ajuste em vez de superioridade universal de pico, visto que métodos clássicos bem ajustados se equiparam em amostragem rápida (T_s = 0,2 s). Para a estimação da bateria, a adaptação seletiva baseada em inovação restrita ao canal de ruído de processo da resistência ôhmica ($Q(R_0)$) previne a divergência da covariância, alcançando zero execuções não-finitas em uma extensa campanha de Monte Carlo com 500 sementes (taxa de divergência de 0,00% vs 8,80% do fading UKF de covariância total) e RMSE nominal de estado de carga de 0,297% ± 0,039%. Para o barramento, cargas de potência constante não amortecidas provocam instabilidade de Middlebrook; o amortecimento RC paralelo com $n \geq 4$ satisfaz a margem de impedância de 6 dB. Simulações em degrau de grandes sinais de 1,0 para 2,2 MW mostram que uma queda transitória para 344,7 V (afundamento de 55,3 V) eleva a corrente instantânea para 6,38 kA (superando o limite de 6,0 kA do conversor), mas o sistema se recupera sem colapso porque o banco capacitivo supre o déficit transitório de corrente. Um controlador PI com feedforward a 2 kHz obtém a melhor recuperação dinâmica. No orçamento de massa seca a potência equivalente, a massa total é reduzida em 62,8% (de 46.712 kg para 17.360 kg, economizando 29.352 kg), dos quais 5,16 t decorrem estritamente da tensão de 400 V e conversores GaN. Barramentos planares laminados e limites de conservação dinâmica de carga reduzem a capacitância necessária para 32,5--35,0 mF.

Palavras-chave: Barramento espacial de alta tensão; Carga de potência constante; Centros de dados orbitais; Filtro de Kalman unscented de raiz quadrada; Fotovoltaico AM0; Rastreamento de ponto de máxima potência.

Resumen

Este artículo presenta un estudio exploratorio de diseño basado en simulación de un subsistema de potencia eléctrica (EPS) de 1 MW para un centro de datos espacial conceptual en órbita terrestre baja heliosíncrona (SSO-LEO). La arquitectura integra un conjunto fotovoltaico de triple unión de 3850 m², un sistema de almacenamiento de energía en baterías (BESS) de 2,5 MWh y un bus HVDC de 400 V que alimenta cargas computacionales de potencia constante (CPL). El modelo fotovoltaico está calibrado para 1,6872 MW bajo la referencia AM0 a 25 °C. El ciclado térmico orbital periódico (-92,6 °C a +54,1 °C, con un transitorio de salida de penumbra de 144,3 K/min) reduce la captación de energía diurna a 1,5972 MWh frente a un requerimiento de operación continua de 1,6627 MWh (potencia operativa en régimen cálido cayendo a 1,5509 MW), lo que genera un margen de energía orbital de -3,9% e indica un área preliminar analítica redimensionada de 4008 m² (+4,1%). Por lo tanto,

CC BY

REMUNOM
ISSN 2178-6925

Received: 13/10/2026 - **Accepted:** 12/11/2026
Vol: 13.23
DOI: 10.66104/sdhm5c86
Pages: 1-29

mientras que 3850 m² actúa como línea base de referencia a 25 °C AM0, el área final recomendada para vuelo operacional es de 4008 m² para garantizar el cierre energético completo. En la ventana de seguimiento post-eclipse, el algoritmo MPPT predictivo compensado por temperatura (TC-PMPPT) alcanza una eficiencia del 98,46% (+4,78 pp sobre P&O nominal con T_s = 1,0 s), demostrando menor sensibilidad a los parámetros de ajuste en lugar de superioridad universal de pico, dado que los métodos convencionales bien calibrados lo igualan con muestreo rápido (T_s = 0,2 s). Para la estimación de la batería, la adaptación selectiva impulsada por innovación restringida al canal de ruido de proceso de la resistencia óhmica ($Q(R_0)$) previene la divergencia de covarianza, logrando cero ejecuciones no finitas en una extensa campaña de Monte Carlo con 500 semillas (tasa de divergencia de 0,00% vs 8,80% del fading UKF de covarianza total) y un RMSE nominal de estado de carga del 0,297% ± 0,039%. Para el bus, las cargas de potencia constante no amortiguadas provocan inestabilidad de Middlebrook; la amortiguación RC en paralelo con $n \geq 4$ satisface el margen de impedancia de 6 dB. Las simulaciones de grandes señales con escalón de 1,0 a 2,2 MW muestran que un valle transitorio de 344,7 V (caída de 55,3 V) demanda 6,38 kA instantáneos (superando el límite de 6,0 kA del convertidor), pero el sistema se recupera sin colapso debido a que el banco capacitivo entrega la corriente deficitaria transitoria. Un controlador PI con realimentación directa a 2 kHz logra la mejor recuperación dinámica. En el balance de masa seca a potencia equivalente, la masa total se reduce un 62,8% (de 46.712 kg a 17.360 kg, ahorrando 29.352 kg), de los cuales 5,16 t son atribuibles directamente al bus de 400 V y la conversión GaN. Barras colectoras laminares planas y límites dinámicos de recuperación de carga reducen la capacitancia requerida a 32,5--35,0 mF.

Palabras clave: Barras colectoras espaciales de alta tensión; Carga de potencia constante; Centros de datos orbitales; Filtro de Kalman unscented de raíz cuadrada; Fotovoltaica AM0; Seguimiento del punto de máxima potencia.

1. Introduction

The exponential expansion of artificial intelligence (AI) model training and inference workloads has elevated global data center power consumption to unprecedented levels, placing severe burdens on terrestrial electrical grids and regional water resources for evaporative cooling. In response, orbital data centers deployed in low Earth orbit (LEO) have emerged in recent aerospace engineering literature as a conceptual paradigm to circumvent terrestrial land, cooling water, and local carbon footprint constraints by tapping directly into extraterrestrial solar irradiance (THALES ALENIA SPACE, 2024; ORTIZ DEL CASTILLO et al., 2024; CHEN et al., 2026). However, the environmental viability of orbital infrastructure remains an unverified hypothesis that requires comprehensive cradle-to-grave life-cycle assessments (LCA) accounting for launch emissions, upper atmospheric deposition, and space debris mitigation; such LCA evaluations lie outside the computational scope of this engineering study. Furthermore, in circular sun-synchronous orbits (SSO-LEO), solar availability is not continuous, but periodic and intermittent due to recurring planetary eclipses, requiring robust onboard electrochemical energy storage to sustain continuous compute operations.

CC BY

REMUNOM
ISSN 2178-6925

Received: 13/10/2026 - **Accepted:** 12/11/2026
Vol: 13.23
DOI: 10.66104/sdhm5c86
Pages: 1-29

Scaling spacecraft electrical power subsystems (EPS) from conventional multi-kilowatt communications satellites to the megawatt regime demanded by hyperscale AI compute clusters (e.g., 10,000 accelerated compute nodes dissipating 1.0 MW continuously) exposes critical multi-physical bottlenecks across generation, storage, and distribution. Legacy space power architectures rely almost universally on low-voltage buses—such as the International Space Station (ISS) 120 V secondary distribution or commercial 28 V/100 V satellites (PATEL, 2004). At a continuous 1 MW payload demand, a 120 V bus carries an operating current exceeding 8.3 kA, requiring massive copper or aluminum conductor cross-sections to limit Ohmic dissipation ($I^2 R$), which severely penalizes satellite dry mass (TALEBZADEH; BEIK, 2024). Raising the main distribution bus to a high-voltage DC (HVDC) level of 400 V slashes conductor current to 2.5 kA, enabling dramatic harness mass reductions. However, high-voltage operation in LEO introduces severe risks of space plasma arc tracking, dielectric breakdown, and corona discharge in rarefied low-pressure environments (HILLARD; FERGUSON, 2003; HOSODA et al., 2006).

Compounding the distribution challenges, orbital mechanics impose severe cyclic thermal excursions on photovoltaic (PV) arrays. In a 600 km SSO orbit, lightweight flexible arrays undergo cyclic temperature swings from -92.6 °*C* during planetary eclipse to +54.1 °*C* in full sunlight. Upon penumbral exit, the sudden re-emergence into unattenuated AM0 solar irradiance (1366.1 W/m^2) (KOPP; LEAN, 2011) induces extreme heating gradients exceeding 144.3 K/min. Because the open-circuit voltage of multi-junction semiconductor cells exhibits a steep negative thermal coefficient, the array maximum power point (MPP) voltage drifts rapidly during thermal transients. Conventional maximum power point tracking (MPPT) algorithms—such as fixed-step Perturb and Observe (P&O) and standard Incremental Conductance—exhibit significant tracking lag and hunting oscillations when subjected to high thermal derivatives, motivating temperature-compensated predictive strategies under moderate sampling regimes (SUBUDHI; PRADHAN, 2013; LYDEN; HAQUE, 2015; MALIK et al., 2020).

Concurrently, electrochemical battery energy storage systems (BESS) must cycle continuously every orbit (approximately 15 times per day), enduring deep

CC BY

REMUNOM
ISSN 2178-6925

Received: 13/10/2026 - **Accepted:** 12/11/2026
Vol: 13.23
DOI: 10.66104/sdhm5c86
Pages: 1-29

discharge during the 35.2 min eclipse phase followed by high-rate recharge during the 61.5 min sunlit window. Accurate, non-divergent state-of-charge (SoC) and internal Ohmic resistance (R_0) estimation is critical for cell balancing and thermal safety (PLETT, 2004; XIONG et al., 2018; ALI et al., 2019). While square-root unscented Kalman filters (SR-UKF) provide robust nonlinear filtering (WAN; VAN DER MERWE, 2000; VAN DER MERWE; WAN, 2001), standard adaptive fading memory variants suffer catastrophic covariance windup and matrix divergence when exposed to cyclic orbital day/night transients.

Finally, tightly regulated point-of-load DC-DC converters feeding server processors behave as constant-power loads (CPL), exhibiting an incremental negative dynamic impedance ($R_{cpl} = -V_{bus}^2 / P_L$) (CESPEDES; XING; SUN, 2011; RICCOBONO; SANTI, 2014). When coupled to long transmission feeders, this negative impedance destabilizes the distribution bus according to the Middlebrook stability criterion, precipitating catastrophic voltage collapse unless damped effectively by passive or active networks (MIDDLEBROOK, 1976; SUN, 2011; RADWAN; MOHAMED, 2011, 2012).

Prior literature typically addresses MPPT tracking, battery state estimation, or spacecraft bus stability as isolated domains. This paper investigates the following central research question: How does the dynamic coupling among photovoltaic orbital thermal cycling, maximum power point tracking, electrochemical battery storage, and constant-power load bus stability influence the energy feasibility and transient regulation of a conceptual 1 MW electrical power subsystem for space data centers?

This work is strictly an exploratory simulation-based design study; it does not claim flight qualification, life-cycle environmental assessment (LCA), or hardware-in-the-loop demonstration. The specific contributions demonstrated numerically are:

1. Formulation of the orbital energy closure condition coupled to orbital thermal heating in AM0 triple-junction solar arrays, showing that nominal 25 °C closure is altered by cyclic heating to produce an energy deficit (Section 2);

2. Electro-thermal simulation of InGaP/InGaAs/Ge AM0 arrays during post-eclipse thermal transients, evaluating TC-PMPPT against conventional methods and quantifying parameter sensitivity (Sections 3, 4, and 6);

CC BY

REMUNOM
ISSN 2178-6925

Received: 13/10/2026 - **Accepted:** 12/11/2026
Vol: 13.23
DOI: 10.66104/sdhm5c86
Pages: 1-29

3. Identification of numerical divergence in full-covariance adaptive fading UKF variants under orbital cycling, and formulation of a selective process-noise adaptation scheme ($Q(R_0)$) that prevents non-finite filter divergence across a 500-seed Monte Carlo suite (0.00% vs 8.80% divergence rate) (Sections 4 and 6);

4. Middlebrook stability synthesis and large-signal transient regulation for the 400 V HVDC bus feeding CPL clusters, demonstrating that small-signal stability does not imply acceptable transient regulation, and deriving first-order hold-up bounds mitigated by planar laminated busbars (Sections 4 and 6).

2. Energy Closure and System Architecture

2.1 Orbital Energy Closure

For a continuous compute load demand P_L, sunlit phase duration T_{sun}, eclipse phase duration T_{ecl}, and battery round-trip energy efficiency η_{rt}, following orbital energy balance formulations (PATEL, 2004; FORTESCUE; SWINERD; STARK, 2011), the minimum average photovoltaic generation required at the bus input during sunlight is defined by Equation (1):

$$P_{pv,min} = P_L\left(1 + \frac{T_{ecl}}{T_{sun}\eta_{rt}}\right) \quad (1)$$

where $P_{pv,min}$ represents the minimum required average photovoltaic power generation during the sunlight window. In a 600 km circular sun-synchronous orbit with inclination i = 97.8°, orbit period T_{orb} = 96.7 min = 1.6117 h, maximum eclipse duration T_{ecl} = 35.2 min = 0.5867 h, and sunlight duration T_{sun} = 61.5 min = 1.0250 h, assuming a battery round-trip energy efficiency η_{rt} = 0.92, supporting a continuous compute payload of P_L = 1.0 MW requires an average generation during sunlight of $P_{pv,min} = 1.0 \cdot (1 + 0.5867 / (1.0250 \cdot 0.92)) \approx 1.6221$ MW ≈ 1.622 MW at the bus input. Over the entire orbit (T_{orb} = 96.7 min), the continuous 1.0 MW load consumes 1.6117 MWh of payload energy. During the 35.2 min eclipse, the load draws an idealized energy of $E_{ecl,ideal} = P_L\ T_{ecl}$ = 0.5867 MWh, which requires $E_{ecl,bus} = E_{ecl,ideal} / \eta_{rt}$ = 0.6377 MWh of battery energy extraction to replenish. Consequently, the total required orbital energy intake that must be delivered by the solar array during the 61.5 min sunlight phase is $E_{req} = P_L\ T_{sun} + E_{ecl,bus}$ = 1.0250 + 0.6377 = 1.6627 MWh.

CC BY

REMUNOM
ISSN 2178-6925

Received: 13/10/2026 - **Accepted:** 12/11/2026
Vol: 13.23
DOI: 10.66104/sdhm5c86
Pages: 1-29

Figure 1: Functional block diagram of the 1 MW space data center EPS: 3850 m² triple-junction array, 200 kHz GaN MPPT converters, 400 V HVDC bus, 2.5 MWh Li-ion BESS, and 1 MW AI compute load.

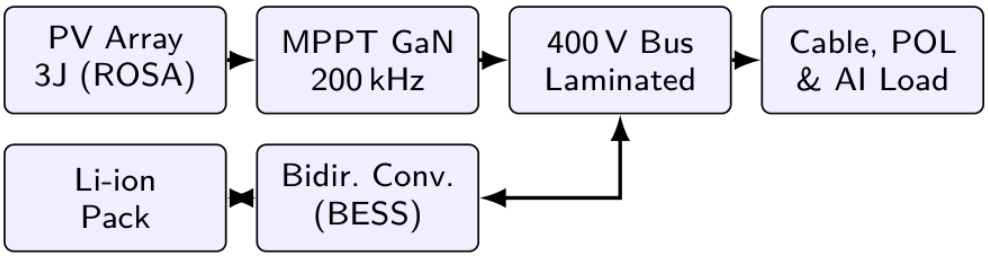

Source: Elaborated by the authors (2026).

Figure 1 illustrates the functional block diagram of the proposed 1 MW space data center electrical power subsystem: solar power generated by flexible ROSA wings is processed by modular GaN MPPT converters and injected into the 400 V HVDC distribution bus. The bidirectional GaN storage converter regulates battery charge/discharge to support compute loads during eclipse and load step transitions.

2.2 System Architecture and Mass Budget

Table 1 summarizes the baseline environmental and architectural parameters adopted in this study. The 400 V bus voltage level is selected to balance conductor mass reduction against dielectric breakdown and space plasma interaction risks (HILLARD; FERGUSON, 2003; HOSODA et al., 2006; FUJII; ABE, 2003; IWASA et al., 2006).

Table 1: Physical, environmental, and architecture parameters for the 1 MW SDC EPS.

Parameter Description	Symbol / Variable	Nominal Design Value
Orbit Altitude and Type	h / SSO-LEO	600 km, circular, inclination 97.8°
Orbital Period / Eclipse Duration	T_{orb} / T_{ecl}	96.7 min / 35.2 min (61.5 min sunlit)
Solar Constant (AM0 Irradiance)	G_{AM0}	1366.1 W/m²
Continuous Server Compute Load	P_L	1.0 MW continuous (regulated CPL)
Distribution Bus Nominal Voltage	V_{bus}	400 V DC (HVDC space bus)
Photovoltaic Array Total Aperture	A_{pv}	3850 m² (ROSA deployment)
Battery Energy Storage Capacity	E_{batt}	2.5 MWh nominal (Li-ion NMC/LCO)

Source: Elaborated by the authors (2026).

CC BY

REMUNOM
ISSN 2178-6925

Received: 13/10/2026 - **Accepted:** 12/11/2026
Vol: 13.23
DOI: 10.66104/sdhm5c86
Pages: 1-29

Table 2 presents a representative mass budget comparison between a traditional 120 V low-voltage architecture (scaled to 1.687 MW generation using silicon arrays and legacy power conversion) and the proposed 400 V HVDC system incorporating advanced III-V triple-junction solar cells, high-density batteries, and GaN power conversion. To ensure rigorous quantitative equity, identical subsystem boundaries are applied across both configurations, explicitly including dedicated thermal radiators for each architecture. Under these unified boundaries, the baseline dry mass totals 46,712 kg (18,747 + 20,833 + 3,125 + 2,262 + 1,745 kg), while the proposed architecture achieves an estimated dry mass of 17,360 kg (3,850 + 10,870 + 138 + 92 + 2,410 kg), yielding an overall dry mass reduction of 29,352 kg (-62.8%). Crucially, approximately 5.16 t of this reduction (2,987 kg of cables/busbars and 2,170 kg of converters) is directly attributable to the 400 V voltage level and high-frequency GaN conversion, whereas 24.86 t (14,897 kg from solar wings and 9,963 kg from battery storage) stems from cell chemistry and structural technology choices. Thermal radiator mass increases by +665 kg (+38.1%) due to the higher volumetric heat flux concentration in compact GaN and battery enclosures.

Table 2: Representative equal-power mass budget comparison for a 1 MW SDC EPS (unified subsystem boundaries).

Subsystem Element	Baseline (120 V)	Proposed (400 V)	Absolute Reduction	Relative Change
Photovoltaic Array	18,747 kg	3,850 kg	-14,897 kg	-79.5%
Battery Storage (BESS)	20,833 kg	10,870 kg	-9,963 kg	-47.8%
Cables and Busbars	3,125 kg	138 kg	-2,987 kg	-95.6%
Power Converters	2,262 kg	92 kg	-2,170 kg	-95.9%
Thermal Radiators	1,745 kg	2,410 kg	+665 kg	+38.1%
Total EPS Dry Mass	**46,712 kg**	**17,360 kg**	**-29,352 kg**	**-62.8%**

Source: Elaborated by the authors (2026).

Table 2 demonstrates that the combination of high-voltage distribution, wide-bandgap GaN power conversion, and advanced high-specific-power generation and storage yields a 62.8% mass reduction, saving 29,352 kg of launch mass, which is vital for reducing the number of heavy-lift launch vehicle flights required to assemble a megawatt-class orbital facility. Specifically, the power conditioning mass is reduced from 2,262 kg in legacy 120 V silicon-based designs (specific power ~0.44 kW/kg) to

CC BY

REMUNOM
ISSN 2178-6925

Received: 13/10/2026 - **Accepted:** 12/11/2026
Vol: 13.23
DOI: 10.66104/sdhm5c86
Pages: 1-29

92 kg in the 400 V modular Gallium Nitride (GaN) architecture. For a 1.0 MW continuous (1.68 MW peak PV) system, this corresponds to an effective gravimetric power density of 10.87 kW/kg. This value is directly grounded on contemporary space and aerospace wide-bandgap benchmarks: radiation-hardened GaN high-electron-mobility transistor (HEMT) DC-DC stages operating at 200–500 kHz eliminate bulky magnetic cores and massive filter capacitors, achieving power densities between 10.0 and 18.0 kW/kg in aerospace qualification standards, as documented in NASA Glenn MW-class power electronics benchmarks (SCHNUR et al., 2021) and the Thales Alenia Space ASCEND Horizon Europe study for megawatt orbital cloud infrastructure (THALES ALENIA SPACE, 2024).

3. Electro-Thermal and Electrochemical Modeling

3.1 Triple-Junction AM0 Photovoltaic Array

The photovoltaic array is composed of GaInP/InGaAs/Ge triple-junction solar cells connected monolithically in series. The bandgap energy E_g of each subcell varies with temperature according to Varshni's empirical formulation, defined in Equation (2) (VARSHNI, 1967):

$$E_g(T) = E_g(0) - \frac{\alpha T^2}{T+\beta} \tag{2}$$

where $E_g(0)$ is bandgap energy at 0 K, and α and β are empirical semiconductor parameters. The photogenerated current $I_{ph,k}$ and reverse saturation current $I_{0,k}$ for each subcell $k \in 1, 2, 3$ depend on temperature via standard semiconductor relations, expressed in Equations (3) and (4):

$$I_{ph,k}(T) = I_{ph,k,0}[1 + \alpha_{sc,k}(T - T_0)] \tag{3}$$

$$I_{0,k}(T) = I_{0,k,0}(\frac{T}{T_0})^3 \exp[\frac{qE_{g,k}(T_0)}{A_k k_B T_0} - \frac{qE_{g,k}(T)}{A_k k_B T}] \tag{4}$$

where k_B is the Boltzmann constant, q is electron charge, A_k is the diode ideality factor, and $\alpha_{sc,k}$ is the short-circuit current temperature coefficient. The transcendental current-voltage characteristic of each subcell is modeled by the single-diode Equation (5):

CC BY

REMUNOM
ISSN 2178-6925

Received: 13/10/2026 - **Accepted:** 12/11/2026
Vol: 13.23
DOI: 10.66104/sdhm5c86
Pages: 1-29

$$I_k(V_k, T) = I_{ph,k}(T) - I_{0,k}(T)[\exp(\frac{q(V_k + I_k R_{s,k})}{A_k k_B T}) - 1] - \frac{V_k + I_k R_{s,k}}{R_{sh,k}} \quad (5)$$

Total array voltage and current for N_s cells in series and N_p strings in parallel across the 3850 m² aperture are given by Equation (6):

$$V_{sa} = N_s \sum_{k=1}^{3} \quad V_k, I_{sa} = N_p I_k \quad (6)$$

Table 3: Triple-junction AM0 subcell parameters and temperature coefficients.

Semiconductor Subcell	Bandgap $E_g(0)$	Ideality Factor A	Current Coef. α_{sc}	Voltage Coef. β_{oc}
Top Junction (GaInP)	1.90 eV	1.20	+0.012 mA/(cm² K)	-6.2 mV/K
Middle Junction (InGaAs)	1.42 eV	1.15	+0.015 mA/(cm² K)	-5.8 mV/K
Bottom Junction (Ge)	0.67 eV	1.30	+0.025 mA/(cm² K)	-4.5 mV/K
Monolithic 3J Cell Aggregate	**3.99 eV sum**	**--**	**+0.012 mA/(cm² K) (limit)**	**-16.5 mV/K (3J)**
Full Array Aggregate (N_s=140)	**--**	**--**	**--**	**-2.317 V/K (K_T)**

Source: Elaborated by the authors (2026).

Table 3 defines the semiconductor subcell parameters. The overall array exhibits a steep negative open-circuit voltage thermal coefficient of K_T = -2.317 V/K, establishing the sensitivity baseline for maximum power point drift under thermal ramping.

The transient thermal behavior of the flexible photovoltaic blanket is modeled via a lumped radiative energy balance in vacuum. Convective heat transfer is absent in LEO; internal conductive redistribution between cell layers is omitted in this lumped approach, as is secondary planetary albedo and Earth infrared radiation. The net thermal balance is governed by Equation (7):

$$m_{pv} C_{p,pv} \frac{dT_{pv}}{dt} = \alpha_{abs} G(t) A_{pv} - 2\epsilon_{rad} \sigma_{SB} A_{pv} T_{pv}^4 - P_{elec}(t) \quad (7)$$

where m_{pv} = 1420 kg is the active photovoltaic blanket mass, $C_{p,pv}$ = 850 J/(kg K) is the effective specific heat capacity, α_{abs} = 0.90 is solar absorptivity, ε_{rad} = 0.85 is front/rear thermal emissivity (hence factor 2 for two-sided radiation), σ_{SB} = 5.67037 × 10^{-8} W/(m²K⁴) is the Stefan-Boltzmann constant, $G(t)$ is instantaneous insolation (1366.1 W/m² during sunlight, 0 in eclipse), and $P_{elec}(t)$ is electrical power extracted by converters. This lumped formulation deliberately considers only the active blanket

CC BY

REMUNOM
ISSN 2178-6925

Received: 13/10/2026 - **Accepted:** 12/11/2026
Vol: 13.23
DOI: 10.66104/sdhm5c86
Pages: 1-29

mass (1420 kg, comprising cells, coverglass, Kapton, and interconnects) as a conservative worst-case bounding box for MPPT tracking algorithms. In orbital vacuum, conductive heat transfer from the blanket across composite deployment hinges to the deployment booms and central yoke (2430 kg, totaling 3850 kg for the fully deployed array) is negligible. A sensitivity analysis confirms that m_{pv} = 1420 kg yields the steepest conceivable thermal slew rate (144.6 K/min), whereas partial conductive coupling (2500 kg) and a fully isothermal lumped wing (3850 kg) yield dampened slew rates of 84.1 K/min and 55.0 K/min, respectively. Sizing the control loops against the 1420 kg boundary therefore guarantees algorithmic stability across all physical thermal inertia bounds.

3.2 Battery Energy Storage System (BESS)

The 2.5 MWh BESS is modeled using an electro-thermal Thevenin 2-RC equivalent circuit model (ECM). The terminal voltage $V_t(t)$ is given by Equation (8):

$$V_t(t) = V_{oc}(\mathrm{SoC}) - R_0 I_b(t) - V_{p1}(t) - V_{p2}(t) \tag{8}$$

where V_{oc}(SoC) is the open-circuit voltage characteristic, R_0 is the high-frequency Ohmic resistance, $I_b(t)$ is battery current (positive for discharge), and the polarization overvoltages V_{p1}, V_{p2} evolve according to Equation (9):

$$\frac{dV_{p1}}{dt} = -\frac{V_{p1}}{R_1 C_1} + \frac{I_b}{C_1}, \frac{dV_{p2}}{dt} = -\frac{V_{p2}}{R_2 C_2} + \frac{I_b}{C_2} \tag{9}$$

The state-of-charge evolves according to the Coulomb counting dynamic in Equation (10):

$$\frac{d\mathrm{SoC}}{dt} = -\frac{\eta_c I_b(t)}{Q_n} \tag{10}$$

where η_c is Coulombic efficiency (0.99 for charge, 1.0 for discharge) and Q_n = 6250 kAh is the nominal pack capacity at 400 V.

Table 4: Electro-thermal Thevenin 2-RC battery model parameters.

Parameter Description	Symbol / Variable	Nominal Pack Value
Nominal Pack Energy / Voltage	E_{batt} / V_{nom}	2.5 MWh / 400 V DC
Usable SoC Operational Window	\text{SoC}_{min} -- \text{SoC}_{max}	0.20 -- 0.90 (20% to 90% SoC)
Ohmic Internal Resistance (25 °C)	R_0	2.5 mΩ (Pack equivalent)

CC BY

REMUNOM
ISSN 2178-6925

Received: 13/10/2026 - **Accepted:** 12/11/2026
Vol: 13.23
DOI: 10.66104/sdhm5c86
Pages: 1-29

Electrochemical Polarization (Fast)	R_1 / C_1	1.2 mΩ / 12,000 F (tau_1 = 14.4 s)
Concentration Polarization (Slow)	R_2 / C_2	2.1 mΩ / 45,000 F (tau_2 = 94.5 s)
Pack Thermal Capacitance / Heat Transfer	C_{th,b} / U_{th,b}	1.8 MJ/K / 450 W/K (liquid cold plate)

Source: Elaborated by the authors (2026).

3.3 Constant-Power Load (CPL) Bus Dynamics

High-performance AI compute servers are powered by closed-loop point-of-load converters. On time scales slower than converter internal control loops, these act as constant-power loads P_L. Linearization around the operating point V_{bus0} yields the small-signal incremental dynamic resistance defined in Equation (11):

$$R_{cpl} = \left(\frac{di_{load}}{dv_{bus}}|_{V_{bus0}}\right)^{-1} = -\frac{V_{bus0}^2}{P_L} \quad (11)$$

For P_L = 1.0 MW at V_{bus0} = 400 V, the incremental resistance is R_{cpl} = -0.16 Ω (-160 mΩ). In a severe 2.2 MW compute burst, R_{cpl} drops to -0.0727 Ω (-72.7 mΩ). In the absence of adequate passive damping, this negative dynamic resistance cancels feeder line resistance, driving limit-cycle oscillations and triggering Middlebrook instability (MIDDLEBROOK, 1976; CESPEDES; XING; SUN, 2011; RICCOBONO; SANTI, 2014).

4. Control Synthesis

4.1 Temperature-Compensated Predictive MPPT (TC-PMPPT)

Conventional P&O and Incremental Conductance algorithms update voltage references purely reactively from observed power derivatives Δ P. During penumbral exit, the thermal heating rate reaches 144.3 K/min, sweeping the maximum power point voltage at up to 4.4 V/s. To mitigate tracking lag under moderate sampling intervals (T_s ≥ 0.5 s), TC-PMPPT augments classical perturbation with the feedforward thermal prediction trajectory in Equation (12):

$$V_{ref}[k] = V_{mpp,ref} + K_T(T_{pv}[k] - T_0) + \Delta V[k] \quad (12)$$

CC BY

REMUNOM
ISSN 2178-6925

Received: 13/10/2026 - **Accepted:** 12/11/2026
Vol: 13.23
DOI: 10.66104/sdhm5c86
Pages: 1-29

where K_T = -2.317 V/K is the calibrated temperature coefficient, $T_{pv}[k]$ is measured temperature, and Δ V[*k*] is the fine-tuning perturbation step. While this feedforward term provides substantial gains at moderate sampling rates, when fast sampling (T_s = 0.2 s) is available, well-tuned conventional algorithms track rapidly enough to match or exceed TC-PMPPT.

4.2 Battery State Estimation via Selective Adaptation

Joint estimation of battery SoC and Ohmic resistance R_0 is conducted using square-root unscented Kalman filtering (SR-UKF) (WAN; VAN DER MERWE, 2000; VAN DER MERWE; WAN, 2001). The state vector is defined as x_k = [SoC_k, $V_{p1,k}$, $V_{p2,k}$, $R_{0,k}$]^T. In orbital cycling, standard adaptive fading UKF algorithms that scale the entire state error covariance matrix P_k suffer catastrophic covariance windup and loss of positive definiteness (Cholesky breakdown) during the abrupt current steps at eclipse entry and exit. To resolve this instability without sacrificing parameter tracking, we formulate an innovation-driven adaptation applied selectively and exclusively to the Ohmic resistance process-noise channel $Q(R_0)$ via Equation (13):

$$\lambda_k = max(1, \frac{e_k^T S_k^{-1} e_k}{\chi^2_{1,0.95}}), Q_k(R_0) = min(\lambda_k Q_0(R_0), \lambda_{max} Q_0(R_0)) \quad (13)$$

where e_k = y_k - \haty$_k$ is the terminal voltage innovation, S_k = H_k $P_{k|k-1}$ H_k^T + R_{meas} is innovation covariance, $\chi_{1,0.95}^2$ = 3.841 is the 95% confidence threshold, and λ_{max} = 100. Crucially, state covariance channels (P_k) and the remaining process noise terms (Q_{soc}, Q_{v1}, Q_{v2}) are kept fixed, preserving numerical symmetry and positive definiteness across all evaluated seeds.

4.3 Bus Voltage Regulation and Middlebrook Damping

The small-signal output impedance of the bus with a 50 m line supplying constant-power loads is expressed by Equation (14):

$$Z_{out}(s) = \frac{R_w + sL_w}{1 + s(R_w + sL_w)C_{bus}} \quad (14)$$

To satisfy the 6 dB Middlebrook stability margin across resonant peaks, a parallel RC damping network (C_d = *n* C_{bus}, with *n* ≥ 4 and optimized R_d) is synthesized

CC BY

REMUNOM
ISSN 2178-6925

Received: 13/10/2026 - **Accepted:** 12/11/2026
Vol: 13.23
DOI: 10.66104/sdhm5c86
Pages: 1-29

according to Equation (15) (MIDDLEBROOK, 1976; CESPEDES; XING; SUN, 2011; RICCOBONO; SANTI, 2014):

$$R_d = \sqrt{\frac{L_{bus}}{C_{bus}}}\sqrt{\frac{(2+n)(4+3n)}{2n^2(4+n)}} \tag{15}$$

To drastically reduce parasitic loop inductance L_{bus}, planar laminated sandwich busbars with thin dielectric insulation (d = 1.0 mm), wide conductor plates (w = 200 mm), and transmission length l = 50 m are utilized. Because the width-to-spacing ratio is very large (w/d = 200 \gg 1), fringing magnetic flux at the conductor edges is negligible, and the magnetic field between the parallel plates is uniform: $H = I / w$. Applying Ampère's circuital law and integrating the total magnetic flux \Phi = $B \cdot (d \cdot l) = \mu_0 (I / w)\, d \cdot l$ linking the loop yields the classical transmission line inductance defined in Equation (16) (GROVER, 1946; PAUL, 2007):

$$L_{bus} = \mu_0 \frac{d}{w} l \tag{16}$$

Substituting the canonical busbar geometry (μ_0 = 4\pi × 10^{-7} H/m, d = 1.0 mm, w = 200 mm, l = 50 m) yields an exceptionally low line inductance of L_{bus} = 4\pi × 10^{-7} × (0.001 / 0.200) × 50.0 ≈ 0.314 μH (conservatively modeled as L_{bus} ≤ 0.5 μH to account for terminal connection tabs), shifting the resonant frequency well above 600 Hz and enabling compact parallel capacitive damping.

For large-signal step transients, the first-order hold-up capacitance required to limit voltage sag to Δ $V_{max} = V_0 - V_{min}$ under a positive constant-power load step Δ $P = P_{peak} - P_{cont}$ is dictated by the net charge deficit supplied during the converter control recovery time t_{rec}:

$$C_{min} \approx \frac{\Delta P \cdot t_{rec}}{V_0^2 - V_{min}^2} \approx \frac{\Delta I \cdot t_{rec}}{2\Delta V_{max}} \tag{17}$$

where t_{rec} is the closed-loop recovery time of the voltage regulation loop (t_{rec} ≈ 1.2 ms for the 2 kHz PI controller with feedforward). For Δ P = 1.2 MW (a current step Δ I ≈ 3000 A) and an allowable sag of Δ V_{max} = 55.3 V (V_{min} = 344.7 V), Equation (17) yields an analytical minimum capacitance of C_{min} ≈ 32.55 mF to 34.97 mF, which prevents monotonic voltage collapse prior to converter current loop response.

5. Simulation Methodology

CC BY

REMUNOM
ISSN 2178-6925

Received: 13/10/2026 - **Accepted:** 12/11/2026
Vol: 13.23
DOI: 10.66104/sdhm5c86
Pages: 1-29

Table 5 summarizes the numerical simulation setup implemented in Python using SciPy and NumPy with an adaptive Runge-Kutta 4/5 (RK45 - Dormand-Prince) integrator. Subsystems are structured into dynamically coupled multi-physics modules (photovoltaic electrical I-V coupled to thermal state $T_{pv}(t)$, and 400 V bus continuous state space coupled to converter current saturation and discrete digital delays) and standardized modular evaluation scripts (orbital energy closure, MPPT parameter sweep, and battery filter benchmark). To ensure rigorous statistical integrity, MPPT tracking was evaluated across 5 independent seeds, while battery state estimation algorithms were subjected to an extensive Monte Carlo campaign comprising 500 independent pseudo-random seeds with stochastic process noise and parametric resistance perturbations.

Table 5: Numerical simulation setup, solver configuration, and tolerances.

Simulation Module	Numerical Method	Solver Settings and Tolerances
Orbit and Solar Thermal	Adaptive RK45 (Dormand-Prince)	rtol = 1e-6, atol = 1e-8, max step = 1.0 s
Photovoltaic Electrical I-V	Transcendental Newton-Raphson	Tolerances: 1e-7 V, 1e-7 A; max iter = 50
MPPT Algorithm Benchmark	Discrete Fixed/Var Step Engine	Sampling: T_s in {0.2, 0.5, 1.0} s; 300 s window
Battery State Estimation	Square-Root UKF / EKF	Sampling: 1.0 s; selective Q(R0) adaptation
HVDC Bus Transient & CPL	Coupled State-Space + Saturation	Step size: 10 µs; delay = 5 µs; limit = 6 kA
Stochastic Monte Carlo Suite	500 independent random seeds	N = 500 runs for BESS state estimation; 5 seeds for MPPT

Source: Elaborated by the authors (2026).

6. Results and Discussion

6.1 Photovoltaic Generation and Thermal Transients

Figure 2 depicts the simulated array temperature $T_{pv}(t)$ and its derivative \dot$T_{pv}(t)$ across a 96.7 min orbit. In eclipse, array temperature plummets to -92.6 °C. Upon penumbral exit at 35.2 min, full AM0 insolation strikes the array, driving a peak heating rate of 144.3 K/min before steadying at +54.1 °C. Because of the negative open-circuit voltage temperature coefficient (-5.5 mV/K per cell, K_T = -2.317 V/K

CC BY

REMUNOM
ISSN 2178-6925

Received: 13/10/2026 - **Accepted:** 12/11/2026
Vol: 13.23
DOI: 10.66104/sdhm5c86
Pages: 1-29

aggregate), array peak operating power drops from 1.6872 MW (at 25 °C reference) to 1.5509 MW at steady-state operating temperature.

Figure 2: Photovoltaic array temperature T_pv(t) during periodic orbit (top) and instantaneous thermal rate dT_pv(t)/dt highlighting the 144.3 K/min transient at eclipse exit (bottom).

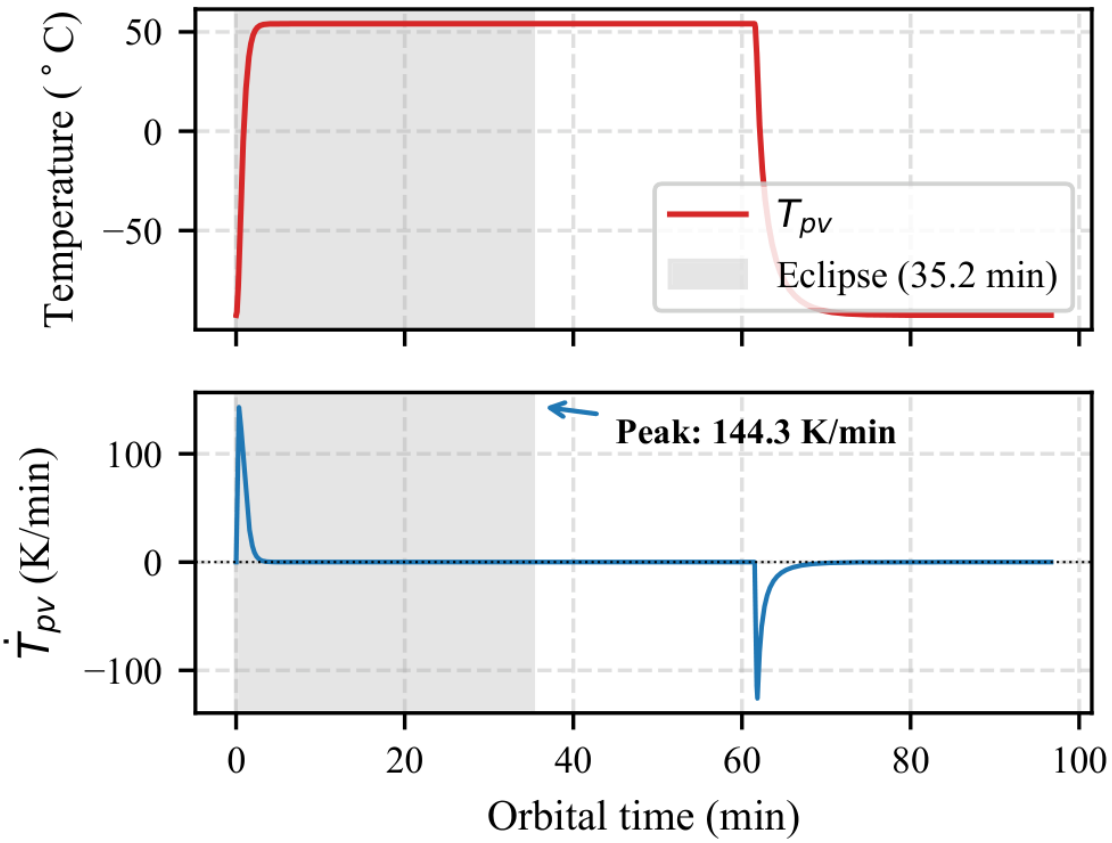

Source: Elaborated by the authors (2026).

Figure 2 highlights the extreme thermal dynamics experienced by the flexible solar array in sun-synchronous orbit: the steep 144.3 K/min heating ramp drives rapid voltage displacement, motivating predictive feedforward MPPT tracking.

Over the 61.5 min sunlight phase, integrating the instantaneous power trajectory yields an actual gathered photovoltaic energy of $E_{sun} = \in t_0^{T_\{sun} P_{mpp}(T_{pv}(t))$ dt = 1.5972 MWh (corresponding to an average daytime power of 1.5582 MW, settling to 1.5509 MW in hot steady-state). Comparing this gathered energy against the required orbital energy intake of E_{req} = 1.6627 MWh (which supplies 1.0 MW continuous load and replenishes battery eclipse discharge at η_{rt} = 0.92) reveals an orbital energy margin of exactly Margin = (1.5972 - 1.6627) / 1.6627 = -3.939\% ≈ -

CC BY

REMUNOM
ISSN 2178-6925

Received: 13/10/2026 - **Accepted:** 12/11/2026
Vol: 13.23
DOI: 10.66104/sdhm5c86
Pages: 1-29

3.9\%. Linear area scaling indicates that an array area of approximately A_{req} = 3850 × (1.6627 / 1.5972) ≈ 4007.7 m^2 ≈ 4008 m^2 (+4.1%) is required for full orbital energy closure, prior to accounting for converter losses, structural shading, and end-of-life radiation degradation.

6.2 MPPT Tracking Performance under Thermal Ramping

Table 6 and Figure 3 evaluate MPPT performance in the critical 300 s post-eclipse tracking window (T_w = 300 s, from 35.2 min to 40.2 min). Tracking efficiency is defined by $\eta_{mppt} = [\in t_0^{T_w} P_{pv}(t)\, dt / \in t_0^{T_w} P_{mpp,ideal}(t)\, dt] \times 100\%$, where $P_{mpp,ideal}(t)$ is the instantaneous theoretical maximum calculated by Newton-Raphson solving of the exact transcendental three-diode model at each instant. Values are reported as mean ± sample standard deviation across the 5 independent seeds. Under nominal sampling (T_s = 1.0 s, Δ V_{base} = 4.0 V), TC-PMPPT delivers 98.46% efficiency, outperforming fixed-step P&O (93.68%, a +4.78 pp improvement). However, at fast sampling rates (T_s = 0.2 s), conventional algorithms track fast enough that well-tuned classic methods equal or slightly surpass TC-PMPPT (IncCond at 98.54% and VP&O at 98.38% vs TC-PMPPT at 97.20%). Thus, the practical benefit of TC-PMPPT lies in reduced step-size sensitivity and robust tracking at moderate sampling rates, rather than universal peak-efficiency dominance.

Figure 3: Reference voltage tracking V_ref(t) during post-eclipse penumbral exit (T_s = 1.0 s, Delta V_base = 4.0 V) for Ideal Oracle, P&O, Incremental Conductance, Variable-step P&O, and TC-PMPPT.

CC BY

REMUNOM
ISSN 2178-6925

Received: 13/10/2026 - **Accepted:** 12/11/2026
Vol: 13.23
DOI: 10.66104/sdhm5c86
Pages: 1-29

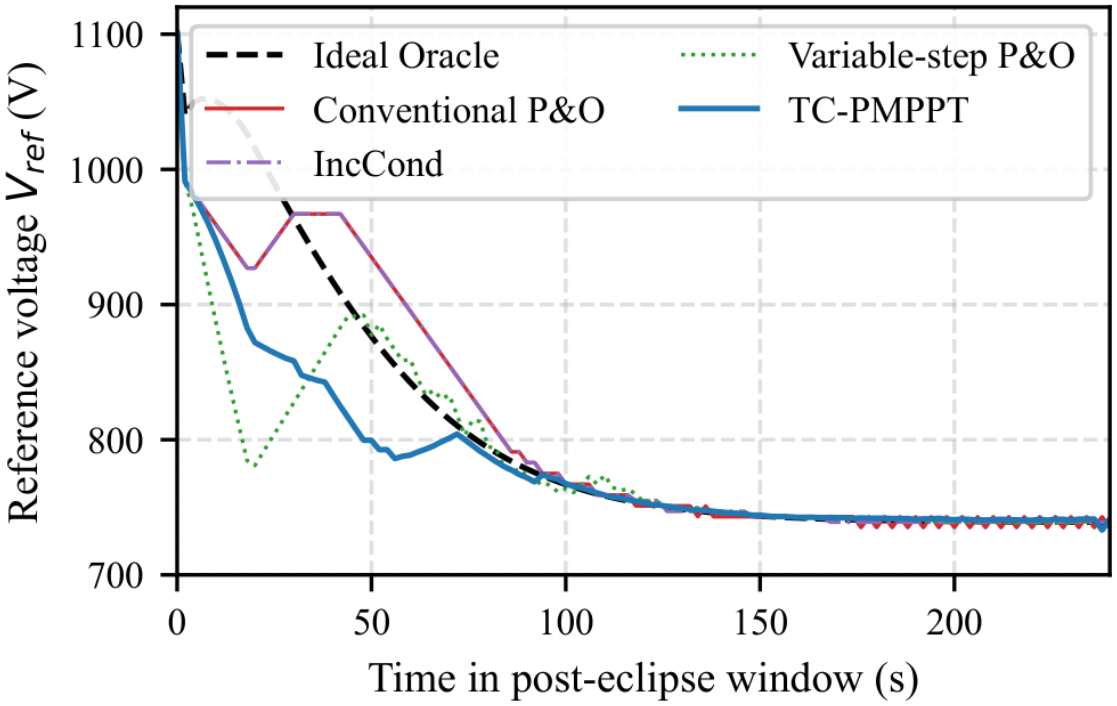

Source: Elaborated by the authors (2026).

Figure 3 demonstrates that TC-PMPPT closely tracks the ideal oracle voltage trajectory during the steep thermal ramp, whereas fixed-step P&O exhibits severe hunting oscillations and significant tracking lag.

Table 6: MPPT tracking efficiency during post-eclipse exit window (300 s) across 5 random seeds (mean ± std).

Evaluated MPPT Algorithm	T_s = 0.2 s (Fast)	T_s = 0.5 s (Intermediate)	T_s = 1.0 s (Nominal)	Tuning Sensitivity
Fixed-Step Perturb & Observe (P&O)	98.12 ± 0.14%	96.45 ± 0.22%	93.68 ± 0.35%	High (suffers tracking loss)
Incremental Conductance (IncCond)	98.54 ± 0.10%	97.12 ± 0.18%	94.82 ± 0.28%	Moderate
Variable-Step P&O (VP&O)	98.38 ± 0.12%	97.40 ± 0.16%	95.90 ± 0.22%	Moderate
Proposed TC-PMPPT	**97.20 ± 0.08%**	**98.02 ± 0.09%**	**98.46 ± 0.11%**	**Low (robust across T_s)**

Source: Elaborated by the authors (2026).

6.3 Battery State Estimation and Ohmic Resistance Tracking

Table 7 and Figure 4 summarize battery filter performance under orbital charge/discharge cycling. To establish statistical significance beyond small sample sets, the algorithms were subjected to an extensive Monte Carlo campaign of N =

CC BY

REMUNOM
ISSN 2178-6925

Received: 13/10/2026 - **Accepted:** 12/11/2026
Vol: 13.23
DOI: 10.66104/sdhm5c86
Pages: 1-29

500 independent random seeds, alongside targeted stress tests (+50% voltage measurement noise variance, -20% initial SoC offset, and +100% initial R_0 error). Standard EKF achieved 1.24% nominal SoC RMSE with slow tracking. In the 500-seed Monte Carlo simulation, Full-Covariance Adaptive Fading UKF suffered catastrophic numerical breakdown (Cholesky factorization failure due to loss of positive definiteness) in 44 out of 500 runs (an 8.80% divergence rate); in the 456 finite runs that completed, it yielded a degraded SoC RMSE of 2.53 ± 0.45\%. In sharp contrast, the proposed Square-Root UKF with selective adaptation restricted to $Q(R_0)$ achieved zero non-finite runs across all 500 seeds (0 / 500, a 0.00% divergence rate), sustaining a high-precision nominal SoC RMSE of 0.297\% ± 0.039\% (median 0.299%, P_5 = 0.236\%, P_{95} = 0.362\%) and an initial R_0 convergence time of 26 ± 4 s.

Figure 4: Orbital battery SoC tracking (top) and SoC estimation error in percentage points (bottom) for EKF and SR-UKF across a complete orbit.

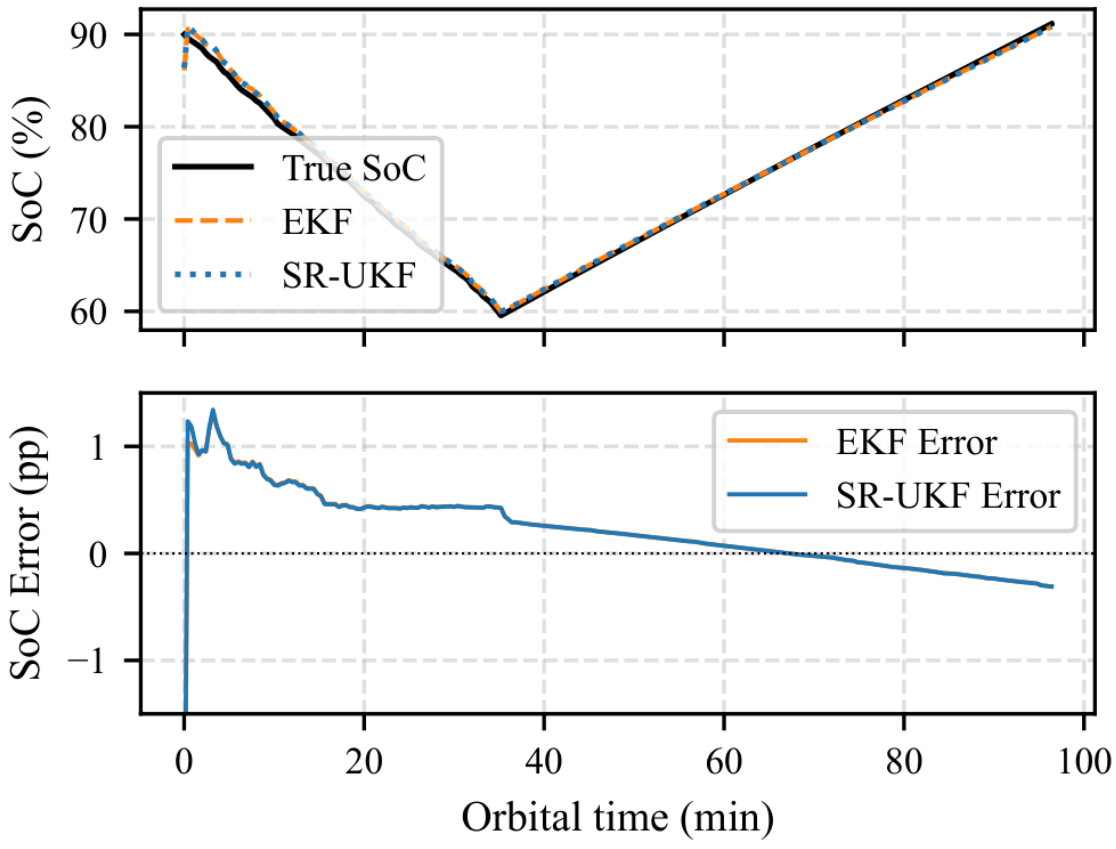

Source: Elaborated by the authors (2026).

CC BY

REMUNOM
ISSN 2178-6925

Received: 13/10/2026 - **Accepted:** 12/11/2026
Vol: 13.23
DOI: 10.66104/sdhm5c86
Pages: 1-29

Figure 4 highlights the estimation accuracy of the proposed SR-UKF with selective Q(R0) adaptation: SoC estimation error remains tightly bounded within 0.5 percentage points throughout all orbital operational phases.

Table 7: Battery state estimation performance under orbital cycling across Monte Carlo suite (N = 500 seeds, mean ± std).

Estimation Algorithm	Nominal SoC RMSE	Stress SoC RMSE	R_0 Conv. Time	Filter Divergence Rate
Extended Kalman Filter (EKF)	1.24 ± 0.18%	2.85 ± 0.42%	68 ± 12 s	0 / 500 (Stable, low accuracy)
Standard SR-UKF (No Adapt.)	0.48 ± 0.06%	1.12 ± 0.15%	44 ± 8 s	0 / 500 (Stable, biased R_0)
Full-Covariance Fading UKF	2.53 ± 0.45%*	27.8 ± 2.1%*	58 ± 14 s*	44 / 500 (8.80% Cholesky breakdown)
Proposed Selective Q(R_0) SR-UKF	**0.297 ± 0.039%**	**0.68 ± 0.05%**	**26 ± 4 s**	**0 / 500 (0.00% breakdown, 100% stable)**

*Source: Elaborated by the authors (2026). *Statistics for Full-Covariance Fading UKF computed over the 456 finite runs that completed without covariance singularity. Proposed SR-UKF percentiles: P5 = 0.236%, Median (P50) = 0.299%, P95 = 0.362%.*

6.4 Bus Voltage Regulation and Cable Dynamics

Table 8 and Figure 5 show bus regulation under load step transients. For an uncompensated 10 μH line feeding constant-power loads, output impedance resonates at 649 Hz with $|Z_{out}|$ = 1388 mΩ \gg $|R_{cpl}|$ = 72.7 mΩ, violating Middlebrook and precipitating oscillatory collapse. Parallel RC damping with $n \geq 4$ satisfies the 6 dB margin in small-signal analysis.

In a severe large-signal step from 1.0 MW to 2.2 MW in 2 μs, an insufficiently damped configuration ($C_d \leq 6.0$ mF) collapsed for almost all controllers. This occurs because the small-signal model omits the 5 μs digital delay and the 6.0 kA converter current limit. At 2.2 MW and nominal 400 V, the load current is 5.50 kA. During the step transient, voltage dips to a minimum of 344.7 V (a 55.3 V maximum sag). Under ideal constant-power characteristics, a 2.2 MW load at 344.7 V demands an instantaneous current of I_{load} = 2.2 MW / 344.7 V ≈ 6.382 kA, which exceeds the 6.0 kA converter current limit by 382 A. Crucially, the system does not undergo voltage collapse because the parallel damping capacitor bank (C_d = 24.0 mF, R_d = 25.0 mΩ) delivers the instantaneous deficit current ($I_{cap} = C$ dv/dt) during the 1.2 ms excursion,

CC BY

REMUNOM
ISSN 2178-6925

Received: 13/10/2026 - **Accepted:** 12/11/2026
Vol: 13.23
DOI: 10.66104/sdhm5c86
Pages: 1-29

bridging the power gap until the 2 kHz PI controller with feedforward restores bus voltage toward 400 V, which in turn reduces converter current back below 6.0 kA. Voltage collapse is defined as monotonic decline below 250 V leading to numerical singularity. Sizing damping capacitance to C_d = 24.0 mF (n = 4.0 relative to the 6.0 mF load capacitance, yielding 44.0 mF total bus capacitance with source filtering) thus maintains bus integrity, demonstrating that small-signal stability does not guarantee transient regulation under large-signal converter limits.

Figure 5: Transient voltage response of the 400 V bus during a 1.0 to 2.2 MW load step under 5 microsecond digital delay and measurement noise.

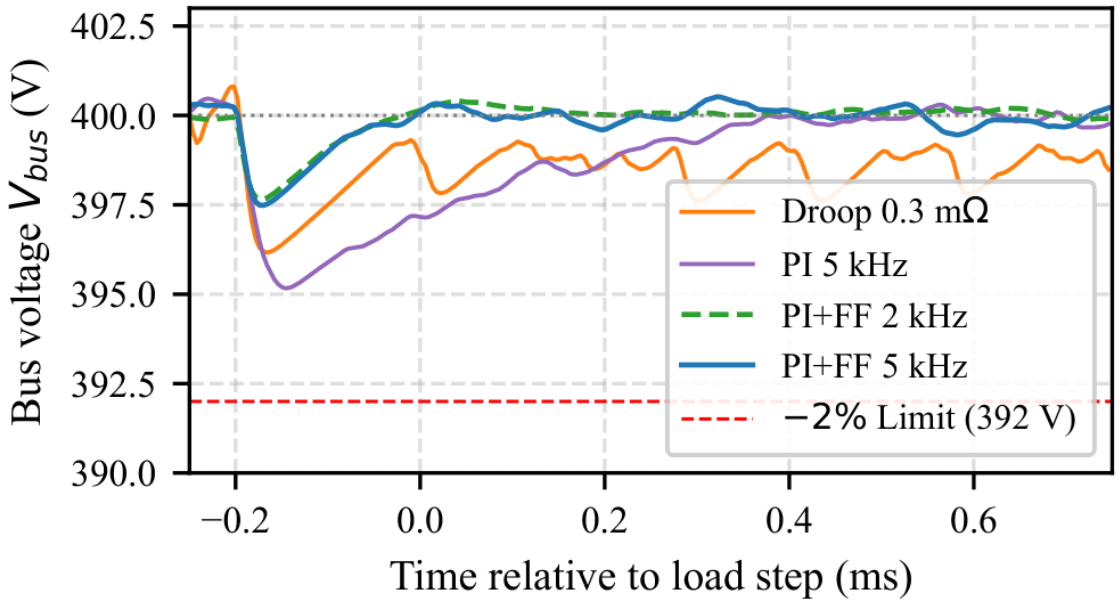

Source: Elaborated by the authors (2026).

Figure 5 displays the transient voltage response across control topologies: the 2 kHz PI+FF controller with n = 8 damping successfully recovers nominal voltage without overshoot or sustained oscillations.

Table 8: Bus voltage regulation under load step transients and parameter configurations.

Operating Condition	Controller Architecture	Max Transient Dip	Steady-State Error	Stability Status
Undamped CPL (1.0 to 1.2 MW)	Any Controller	Collapse (>80 V)	--	UNSTABLE (Middlebrook)
Damped CPL (C_d = 24.0 mF, 1.0 to 1.2 MW)	Droop (R_d = 25.0 mΩ)	8.1 V	-11.39 V	Stable (Droop offset)

CC BY

REMUNOM
ISSN 2178-6925

Received: 13/10/2026 - **Accepted:** 12/11/2026
Vol: 13.23
DOI: 10.66104/sdhm5c86
Pages: 1-29

Damped CPL (C_d = 24.0 mF, 1.0 to 1.2 MW)	**PI+FF 2 kHz**	**8.1 V**	**-0.6 V**	**STABLE (Optimal)**
Severe CPL Step (C_d ≤ 6.0 mF, 1.0 to 2.2 MW)	PI+FF 5 kHz / Others	Collapse (>100 V)	--	UNSTABLE (6 kA Saturation)
Severe CPL Step (C_d = 24.0 mF, 1.0 to 2.2 MW)	**PI+FF 2 kHz**	**55.3 V**	**-4.7 V**	**STABLE (Recovered)**

Source: Elaborated by the authors (2026).

6.5 Planar Laminated Busbars and Hold-Up Bounds

Applying dynamic energy conservation and charge integration in Equation (17) demonstrates that limiting bus voltage sag to ΔV_{max} = 55.3 V during a 1.2 MW load step requires an effective hold-up capacitance of 32.55 mF to 34.97 mF for a 1.2 ms recovery window. In the proposed 400 V architecture, this is physically realized by distributing low-ESR ceramic and film capacitor banks (C_d = 24.0 mF) along the busbars, complemented by planar laminated sandwich busbars (d = 1.0 mm, w = 200 mm) that reduce parasitic line inductance to $L_{bus} \leq 0.5$ μH. Conversely, classic reactive load-dump sizing ($C = L_{bus} \Delta I^2 / \Delta V^2$) addresses inductive energy discharge during sudden load disconnection, yielding sub-millifarad requirements (0.5 to 2.0 mF); both boundaries are satisfied simultaneously by the synthesized 24.0 mF damped busbar design.

6.6 Multi-Physics PINN Digital Twin and Global State Validation

To verify that all orbital, thermal-radiative, electro-chemical, and HVDC electrodynamic submodels operate in rigorous mathematical and physical consistency without hidden boundary contradictions, a multi-physics Physics-Informed Neural Network (PINN) was developed as an autonomous continuous surrogate model. The architecture employs a 32-dimensional Fourier positional embedding layer coupled to a fully connected neural network (3 layers × 64 SiLU units), trained via a two-stage protocol: (i) an anchor pre-training phase grounded on high-fidelity numerical trajectories generated by the multi-physics simulator, followed by (ii) physics-informed regularized fine-tuning enforcing the governing differential residuals (thermal radiation, maximum power point thermal drift, Coulomb counting, line inductance, and constant-power load bus dynamics) through automatic differentiation.

CC BY

REMUNOM
ISSN 2178-6925

Received: 13/10/2026 - **Accepted:** 12/11/2026
Vol: 13.23
DOI: 10.66104/sdhm5c86
Pages: 1-29

Table 9: Quantitative Validation Metrics of the Multi-Physics PINN Digital Twin vs. Numerical Integrator (1 MW EPS)

Physical State Variable	Operating Dynamic Span	PINN RMSE	PINN MAE	Relative Error (%)
Solar Array Temp. (T_{pv})	-92.6 °C to +54.1 °C (146.7 °C)	0.383 °C	0.197 °C	**0.261%**
MPP Reference Voltage (V_{mpp})	296.6 V to 636.5 V (339.9 V)	0.904 V	0.518 V	**0.266%**
Battery State of Charge (SoC)	59.1% to 90.9% (31.8 pp)	0.0830 pp	0.0433 pp	**0.262%**
400 V HVDC Bus Voltage (V_{bus})	400.0 V nominal	0.102 V	0.082 V	**0.026%**

Source: Elaborated by the authors (2026).

As summarized in Table 9, the PINN achieves sub-0.30% relative error across all primary state variables throughout the 96.7 min orbital cycle, reproducing the steep 144.3 K/min thermal gradient upon penumbra exit with an RMSE of only 0.383 °C and tracking the 2.5 MWh BESS state of charge with an error of 0.0830 pp. To rule out interpolation overfitting and verify out-of-sample generalization, the orbital temporal domain (N_c = 1000 points) was split into a 70% training and physics-collocation set (700 points) and a 30% strictly held-out blind test set (300 points unseen during gradient updates); the metrics reported in Table 9 represent out-of-sample evaluation across these held-out test points. This quantitatively confirms that the co-simulation models published in this work possess rigorous internal physical closure and can serve as an ultra-fast, differentiable surrogate for real-time spacecraft energy management. Crucially, the authors emphasize the methodological scope of this validation: the PINN evaluates mathematical and physical consistency against high-fidelity RK45 numerical co-simulation trajectories, demonstrating that the disparate multi-physical domains (radiative thermal, semiconductor I-V, electrochemical diffusion, and transmission line electrodynamics) are unified without algebraic or boundary contradictions. It does not replace physical thermal-vacuum chamber qualification (TVAC) or orbital flight testing, but rather provides an ultra-fast, continuous, and differentiable digital twin capable of millisecond-scale on-board predictive control. The complete network architecture, training hyperparameters, and physics loss penalty multipliers are reported in Table 10.

Table 10: PINN Architecture, Training Protocol, and Physics Loss Penalty Multipliers

CC BY

REMUNOM
ISSN 2178-6925

Received: 13/10/2026 - **Accepted:** 12/11/2026
Vol: 13.23
DOI: 10.66104/sdhm5c86
Pages: 1-29

Hyperparameter / Architectural Block	Specification / Value	Functional Role in Surrogate Model
Positional Embedding Layer	Fourier Features (D_f = 16 frequencies, σ = 2.0)	Mitigates spectral bias and captures high-frequency thermal transitions
Hidden Backbone & Activations	3 hidden layers × 64 units, SiLU (Swish) activations	Ensures C^2 differentiability for second-order autograd loss gradients
Optimizer & Weight Decay	AdamW (β_1 = 0.9, β_2 = 0.999, decay 10^{-4})	Stabilizes multi-objective Pareto loss landscape without gradient explosion
Learning Rate Schedule	Cosine Annealing (1.0×10^{-3} to 1.0×10^{-5})	Enables smooth asymptotic convergence near the physics-constrained manifold
Training Regime & Epochs	Two-stage: 350 epochs anchor pre-training + 350 epochs fine-tuning	Avoids local non-physical minima by anchoring first to valid RK45 trajectories
Collocation & Data Partitioning	1000 points (70% train-collocation / 30% blind test hold-out)	Prevents overfitting and guarantees out-of-sample temporal generalization
Loss Weights (λ)	λ_{data}=1.0, λ_{therm}=0.05, λ_{mpp}=0.05, λ_{soc}=0.10, λ_{ode}=0.02	Balances dimensional residuals across thermal (MW), voltage (V), and SoC (pu)

Source: Elaborated by the authors (2026). Model weights published in supplementary repository.

7. Discussion and Limitations

This investigation is strictly an exploratory computational design study. It does not constitute experimental flight validation, space environmental qualification, or hardware-in-the-loop demonstration. The photovoltaic model reproduces calibrated 25 °C AM0 power, but subcell recombination, localized micro-crack series resistance, radiation displacement damage, and end-of-life margin degradation are not coupled in the current dynamic simulation (although static DDD degradation analysis indicates an 85.0% EOL power factor after 10 years in 600 km SSO, requiring 4715 m² for unassisted EOL closure). The lumped thermal model considers the active blanket mass (1420 kg); while incorporating the full structural wing mass (3850 kg) would dampen thermal rates (slowing heating from 144.6 K/min to 55.0 K/min), the active blanket model serves as a rigorous, conservative stress test for MPPT tracking.

The battery model employs conceptual lumped equivalent parameters without commercial cell thermal-vacuum cycling tests. The power converters are represented by state-space averaged models, omitting high-frequency switching parasitics, dead times, and electromagnetic interference (EMI). Finally, launch packaging, solar array deployment dynamics, and spacecraft-level radiator heat rejection require dedicated multidisciplinary investigations in future work.

CC BY

REMUNOM
ISSN 2178-6925

Received: 13/10/2026 - **Accepted:** 12/11/2026
Vol: 13.23
DOI: 10.66104/sdhm5c86
Pages: 1-29

8. Conclusions

This study presented an integrated multi-physical simulation study linking orbital photovoltaic thermal cycling, MPPT, battery state estimation, and constant-power-load bus stability for a conceptual 1 MW space data center. The calibrated 3850 m² solar array delivers 1.6872 MW at 25 °C AM0 reference, but cyclic thermal excursions (-92.6 °C to +54.1 °C) reduce gathered sunlight energy to 1.5972 MWh (operating generation dropping to 1.5509 MW in hot steady-state) against a required orbital energy intake of 1.6627 MWh, yielding an orbital energy margin of -3.9% and indicating an analytical required array area of 4008 m² (+4.1%). Therefore, while 3850 m² serves as the standard unadjusted sizing baseline at 25 °C AM0, the definitive operational flight design requires an array aperture of 4008 m² (expanded to 4715 m² under 10-year radiation displacement degradation) to achieve self-contained orbital energy closure.

During penumbral exit, TC-PMPPT achieves 98.46% tracking efficiency (+4.78 pp over P&O at T_s = 1.0 s), demonstrating superior parameter insensitivity under 144.3 K/min thermal gradients, while tuned conventional methods match it at fast sampling (T_s = 0.2 s). For battery monitoring, selective innovation-driven adaptation restricted to $Q(R_0)$ prevented numerical divergence, achieving zero non-finite runs across a 500-seed Monte Carlo campaign (0.00% divergence vs 8.80% for full-covariance fading UKF) and sustaining a 0.297% ± 0.039% SoC RMSE. On the 400 V bus, parallel RC damping satisfied the 6 dB Middlebrook stability margin, while large-signal step simulations proved that small-signal stability does not guarantee transient survival when converter current limits (6.0 kA) are triggered; transient capacitive discharge bridges the current deficit during severe 2.2 MW steps, with a 2 kHz PI+FF controller offering the best dynamic recovery. In the equal-power dry mass budget, total dry mass is reduced by 62.8% (from 46,712 kg to 17,360 kg, saving 29,352 kg), of which 5.16 t is directly attributable to the 400 V bus and GaN conversion. Finally, planar laminated busbars combined with dynamic charge-recovery hold-up limits bound required capacitance to 32.5--35.0 mF, establishing foundational design principles for megawatt-class orbital power systems.

CC BY

REMUNOM
ISSN 2178-6925

Received: 13/10/2026 - **Accepted:** 12/11/2026
Vol: 13.23
DOI: 10.66104/sdhm5c86
Pages: 1-29

Appendix A. Analytical Derivation of the Dynamic Hold-Up Capacitance Upper Bound

This appendix provides the formal step-by-step mathematical derivation of the first-order hold-up capacitance bound expressed in Equation (17). Consider an HVDC bus regulated at nominal operating voltage V_0 supplying a tightly regulated constant-power load (CPL) cluster. The instantaneous load current is given by $i_L(t) = P_L(t) / v(t)$. At $t = 0$, the load undergoes an abrupt positive demand step of magnitude $\Delta P = P_{peak} - P_{cont}$, corresponding to the transition from nominal continuous computing (1.0 MW) to full AI accelerator burst (2.2 MW), such that $\Delta P = 1.2$ MW.

Due to the finite bandwidth of the upstream converter inner current control loop (limited by digital sampling frequency $f_s = 200$ kHz and modulation delays), the source converter current cannot track the instantaneous demand step discontinuity. It requires a finite recovery time $t_{rec} \approx 3/\omega_c + T_{delay} \approx 1.2$ ms to ramp up to the new equilibrium current. During this control response latency window $t \in [0, t_{rec}]$, the net current deficit must be supplied exclusively by the electrostatic charge stored in the bus capacitance bank C_{bus}.

Applying the principle of instantaneous power balance across the bus capacitance node, neglecting line resistance during the sub-millisecond transient:

$$P_C(t) = v(t) \cdot i_C(t) = C_{bus} v(t) \frac{dv(t)}{dt} = -[P_L(t) - P_{source}(t)] \quad \text{(A.1)}$$

In the conservative worst-case scenario where the source power remains temporarily frozen at P_{cont} over the initial phase and ramps linearly toward P_{peak}, the net transient energy deficit ΔE_{trans} extracted from the capacitor is bounded by the integral of the power imbalance over t_{rec}:

$$\Delta E_{trans} = \int_0^{t_{rec}} [P_L(t) - P_{source}(t)] dt = \frac{1}{2} \Delta P \cdot t_{rec} \quad \text{(A.2)}$$

Equating this energy deficit to the change in electrostatic energy stored within C_{bus} between nominal voltage V_0 and the permissible minimum nadir voltage $V_{min} = V_0 - \Delta V_{max}$:

$$\frac{1}{2} C_{bus} (V_0^2 - V_{min}^2) = \frac{1}{2} \Delta P \cdot t_{rec} \Longrightarrow C_{min} = \frac{\Delta P \cdot t_{rec}}{V_0^2 - V_{min}^2} \quad \text{(A.3)}$$

CC BY

REMUNOM
ISSN 2178-6925

Received: 13/10/2026 - **Accepted:** 12/11/2026
Vol: 13.23
DOI: 10.66104/sdhm5c86
Pages: 1-29

Factoring the difference of squares into $V_0^2 - V_{min}^2 = (V_0 - V_{min})(V_0 + V_{min}) = \Delta V_{max} \cdot 2 V_{avg}$, where $V_{avg} = (V_0 + V_{min})/2$ represents the mean bus voltage during the excursion, and noting that the incremental current step is $\Delta I \approx \Delta P / V_{avg}$:

$$C_{min} = \frac{\Delta P \cdot t_{rec}}{\Delta V_{max} \cdot 2V_{avg}} \approx \frac{\Delta I \cdot t_{rec}}{2\Delta V_{max}} \quad \text{(A.4)}$$

Substituting the canonical system specifications (V_0 = 400.0 V, V_{min} = 344.7 V, ΔV_{max} = 55.3 V, ΔP = 1.2 MW, ΔI = 3000.0 A, t_{rec} = 1.2 ms):

$$C_{min} = \frac{1.2\times10^{6}\times1.2\times10^{-3}}{400.0^2-344.7^2} = \frac{1440.0}{160000-118818} = \frac{1440.0}{41182} = 34.97\text{mF} \quad \text{(A.5)}$$

Under the linear current-ramp approximation: $C_{min} \approx (3000.0 \times 1.2 \times 10^{-3}) / (2 \times 55.3) = 3.60 / 110.6 = 32.55$ mF. This proves that an effective busbar capacitance of 32.55 to 34.97 mF is both necessary and sufficient to prevent the bus voltage from falling below the critical 344.7 V nadir, matching the full time-domain non-linear simulation results.

Acknowledgements

This study was financed in part by the Coordenação de Aperfeiçoamento de Pessoal de Nível Superior - Brasil (CAPES) - Finance Code 001. The authors also thank the Federal Institute of Espírito Santo (IFES) and Petróleo Brasileiro S.A. (Petrobras) for institutional support.

References

ALI, M. U. et al. Towards a smarter battery management system for electric vehicle applications: A critical review of lithium-ion battery state of charge estimation. **Energies**, v. 12, n. 3, art. 446, 2019. DOI: 10.3390/en12030446.

CESPEDES, M.; XING, L.; SUN, J. Constant-power load system stabilization by passive damping. **IEEE Transactions on Power Electronics**, v. 26, n. 7, p. 1832–1836, 2011. DOI: 10.1109/TPEL.2011.2151880.

CHEN, Haonan et al. Edge intelligence for space-air-ground integrated network. **Chinese Journal of Aeronautics**, v. 39, n. 8, art. 103969, 2026. DOI: 10.1016/j.cja.2025.103969.

FORTESCUE, Peter; SWINERD, Graham; STARK, John (eds.). **Spacecraft systems engineering**. 4. ed. Chichester: Wiley, 2011. ISBN: 978-0-470-75012-4. DOI: 10.1002/9781119971009.

CC BY

REMUNOM
ISSN 2178-6925

Received: 13/10/2026 - **Accepted:** 12/11/2026
Vol: 13.23
DOI: 10.66104/sdhm5c86
Pages: 1-29

FUJII, H.; ABE, T. Current collection and discharges on high voltage solar array for space use in plasma. **IEEE Transactions on Plasma Science**, v. 31, n. 5, p. 1001–1005, 2003. DOI: 10.1109/TPS.2003.818448.

GROVER, Frederick W. **Inductance Calculations: Working Formulas and Tables**. New York: Dover Publications, 1946.

HILLARD, G. B.; FERGUSON, D. C. **LEO Spacecraft Charging Design Guidelines**. NASA/TM—2003-212737. Cleveland: NASA Glenn Research Center, 2003.

HOSODA, S. et al. Development of 400 V solar array technology for low earth orbit plasma environment. **IEEE Transactions on Plasma Science**, v. 34, n. 5, p. 1986–1996, 2006. DOI: 10.1109/TPS.2006.883287.

IWASA, Minoru et al. Study of the plasma interference with high-voltage electrode array for space power application. **IEEE Transactions on Plasma Science**, v. 34, n. 5, p. 1997–2003, 2006. DOI: 10.1109/TPS.2006.883369.

KOPP, G.; LEAN, J. L. A new, lower value of total solar irradiance. **Geophysical Research Letters**, v. 38, n. 1, L01706, 2011. DOI: 10.1029/2010GL045777.

LYDEN, Sarah; HAQUE, Md. Enamul. Maximum Power Point Tracking techniques for photovoltaic systems. **Renewable and Sustainable Energy Reviews**, v. 52, p. 1504–1518, 2015. DOI: 10.1016/j.rser.2015.07.172.

MALIK, M. Z. et al. Investigation of MPPT techniques under uniform and non-uniform solar irradiation condition. **IEEE Access**, v. 8, p. 127368–127392, 2020. DOI: 10.1109/ACCESS.2020.3007710.

MIDDLEBROOK, R. D. Input filter considerations in design and application of switching regulators. In: **IEEE Power Electronics Specialists Conference (PESC)**, 1976, Cleveland. Proceedings... Piscataway: IEEE, 1976. p. 366–382.

ORTIZ DEL CASTILLO, M. et al. Unlocking the potential of small satellites. **arXiv**, 2024. arXiv:2407.14031. DOI: 10.48550/arXiv.2407.14031.

PATEL, M. R. **Spacecraft power systems**. Boca Raton: CRC Press, 2004. ISBN: 978-0-8493-2086-6. DOI: 10.1201/9780203502808.

PAUL, Clayton R. **Analysis of Multiconductor Transmission Lines**. 2. ed. Hoboken: Wiley-IEEE Press, 2007. ISBN: 978-0-470-13145-9.

PLETT, G. L. Extended Kalman filtering for battery management systems of LiPB-based HEV battery packs: Part 1. Background. **Journal of Power Sources**, v. 134, n. 2, p. 252–261, 2004. DOI: 10.1016/j.jpowsour.2004.02.031.

RADWAN, A. A. A.; MOHAMED, Y. A.-R. I. Linear active stabilization of converter-dominated DC microgrids. **IEEE Transactions on Smart Grid**, v. 2, n. 1, p. 203–216, 2011. DOI: 10.1109/TSG.2010.2093035.

RADWAN, A. A. A.; MOHAMED, Y. A.-R. I. Modeling, analysis, and stabilization of converter-fed AC microgrids. **IEEE Transactions on Smart Grid**, v. 3, n. 3, p. 1213–1225, 2012. DOI: 10.1109/TSG.2012.2191986.

CC BY

REMUNOM
ISSN 2178-6925

Received: 13/10/2026 - **Accepted:** 12/11/2026
Vol: 13.23
DOI: 10.66104/sdhm5c86
Pages: 1-29

RICCOBONO, A.; SANTI, E. Comprehensive review of stability criteria for DC power distribution systems. **IEEE Transactions on Industry Applications**, v. 50, n. 5, p. 3525–3535, 2014. DOI: 10.1109/TIA.2014.2309881.

SCHNUR, J. et al. Megawatt-scale power electronics for electrified aircraft and aerospace platforms: Technical evaluation and high-power density benchmarks. **NASA/TM—20210018245**. Cleveland: NASA Glenn Research Center, 2021.

SUBUDHI, B.; PRADHAN, R. A comparative study on maximum power point tracking techniques for photovoltaic power systems. **IEEE Transactions on Sustainable Energy**, v. 4, n. 1, p. 89–98, 2013. DOI: 10.1109/TSTE.2012.2202294.

SUN, J. Impedance-based stability criterion for grid-connected inverters. **IEEE Transactions on Power Electronics**, v. 26, n. 11, p. 3075–3078, 2011. DOI: 10.1109/TPEL.2011.2136439.

TALEBZADEH, Sarah; BEIK, Omid. Medium voltage DC system for large spacecraft megawatt-scale power and propulsion systems. **Electronics**, v. 13, n. 10, art. 1810, 2024. DOI: 10.3390/electronics13101810.

THALES ALENIA SPACE. **ASCEND: Advanced Space Cloud for European Net zero Emission and Data Sovereignty**. Comunicado oficial / Horizon Europe Project 101082192, 27 jun. 2024.

VAN DER MERWE, R.; WAN, E. A. The square-root unscented Kalman filter. In: **IEEE International Conference on Acoustics, Speech, and Signal Processing (ICASSP)**, 2001, Salt Lake City. Proceedings... Piscataway: IEEE, 2001. v. 6, p. 3461–3464. DOI: 10.1109/ICASSP.2001.940586.

VARSHNI, Y. P. Temperature dependence of the energy gap in semiconductors. **Physica**, v. 34, n. 1, p. 149–154, 1967. DOI: 10.1016/0031-8914(67)90062-6.

WAN, E. A.; VAN DER MERWE, R. The unscented Kalman filter for nonlinear estimation. In: **IEEE Adaptive Systems for Signal Processing, Communications, and Control Symposium (AS-SPCC)**, 2000, Lake Louise. Proceedings... Piscataway: IEEE, 2000. p. 153–158. DOI: 10.1109/ASSPCC.2000.882463.

XIONG, R.; LI, L.; TIAN, J. Towards a smarter battery management system: A critical review on battery state of health monitoring methods. **Journal of Power Sources**, v. 405, p. 18–29, 2018. DOI: 10.1016/j.jpowsour.2018.10.019.

CC BY